Development of a cloud detection method from whole-sky color images

Masanori Yabuki [a],[*], Masataka Shiobara [b],[c], Kimiko Nishinaka [d], Makoto Kuji [d]

[a] *Research Institute for Sustainable Humanosphere, Kyoto University, Uji, Kyoto 611—0011, Japan*
[b] *National Institute of Polar Research, Tachikawa Tokyo 190—8518, Japan*
[c] *Department of Polar Science, The Graduate University for Advanced Studies, Tachikawa, Tokyo 190-8518, Japan*
[d] *Nara Women's University, Nara, Nara 630—8506, Japan*

Abstract

A method is proposed for detecting clouds from whole-sky color images obtained with an all-sky camera (ASC) system. In polar regions, cloud detection using whole-sky images usually suffers from large uncertainties in fractional cloud cover retrievals because of large solar zenith angles (SZAs) and high surface albedo, which cause "whitening" in the images. These problems are addressed by using differences between real images and virtual clear-sky images for a particular observation time with the same SZA. The method is applied to ASC images obtained at Ny-Ålesund, Svalbard in May of 2005—2007, and the results are compared with Micro-Pulse Lidar (MPL) measurements. When no clouds were detected by MPL, the false cloud detection rate from ASC classification was 2.1% in total hours. Conversely, when clouds were detected by MPL, the ASC classification underestimated the clouds by 11.6%. In most cases, this occurred when MPL detected very optically thin clouds. Furthermore, the variability of cloud fractions estimated by MPL and ASC was roughly constant regardless of the SZA. Thus, it is confirmed that the method developed in this study is valid for cloud detection from whole-sky color images.
© 2014 Elsevier B.V. and NIPR. All rights reserved.

1. Introduction

Clouds play a key role in the earth's radiation budget, by reflecting incoming solar radiation and trapping outgoing radiation. Analyses of satellite remote sensing data indicate that, in polar regions, the warming effect of clouds is larger than the cooling effect; however, the opposite is true in mid- and lower latitudes (Hartmann, 1993). However, passive satellite sensors cannot accurately identify clouds over polar regions, which hampers the investigation of the effects of clouds on the radiation budget (Raschke et al., 2005). Recently, space-borne and ground-based active remote sensors such as radar and lidar have revealed detailed vertical profiles of ice and water clouds, and have been used to investigate profiles of radiative heating rate (e.g., Thorsen et al., 2013). Active remote sensors can only provide detailed vertical profiles at nadir or zenith, but stratiform clouds such as Arctic

---

stratus clouds can extend over several hundreds of kilometers. Therefore, optical imaging sensors should be used in combination with active sensors to monitor extended cloud systems, because the amount and altitude of clouds are key properties for determining the magnitude of radiative effects.

Whole-sky imaging is more useful than zenith observations for cloud determination, because the field of view of the sky camera corresponds to the conventional sky-type observations of meteorological observers. Ground-based sky imaging systems have commonly been used to obtain continuous information about cloud distributions by measuring sky radiance at visible and/or near infrared wavelengths (e.g., Shields et al., 1998, 2013; Feister et al., 2010; Liu et al., 2013). Recently, new methodologies have led to improvements in cloud classification. Heinle et al. (2010) constructed an automatic cloud classification algorithm based on a set of mainly statistical features describing the color and texture of an image. This algorithm employs the k-nearest-neighbor classifier, because of its high performance, simplicity of implementation, and low computational complexity. Heinle et al. (2010) distinguished between seven different sky conditions: high thin clouds (cirrus and cirrostratus), high patchy cumuliform clouds (cirrocumulus and altocumulus), stratocumulus clouds, low cumuliform clouds, thick clouds (cumulonimbus and nimbostratus), stratiform clouds, and clear sky. An improved cloud classification algorithm, based on the work of Heinle et al. (2010), which includes a metric for the existence of rain in digital images, was developed and demonstrated by Kazantzidis et al. (2012).

In this paper, we focus on daytime color whole-sky images divided into three components: red, green, and blue. In general, cloud detection methods are valid for whole-sky images with a high color contrast between a clear sky and clouds. In most cases, image processing algorithms have been developed to estimate cloud fractions by reasoning that the ratio or difference between red and blue color intensities reflects differences in the wavelength dependence of the scattered light between air molecules and clouds (e.g., Long et al., 2006; Heinle et al., 2010). However, Long et al. (2006) stated that using a unique threshold of the red–blue ratio can result in problems with, for example, misdetection of thin clouds in circumsolar pixels in high aerosol conditions. Such pixels are often whiter and brighter than the rest of the hemisphere because of forward scattering by aerosols and haze. Kazantzidis et al. (2012) reported that the use of a red–blue intensity ratio or difference results in errors for cases of broken cloud or overcast conditions at large solar zenith angles (SZAs). They proposed a multi-color threshold that also takes into account the green intensity of the image for discriminating cloud areas. Alonso et al. (2014) used direct normal irradiance to correctly identify the solar disk, to resolve the problem related to the saturation of pixels in images from sky cameras being used to detect clouds.

In polar regions, cloud detection using whole-sky images usually suffers from large uncertainties because of the large SZAs, as well as the high surface albedo, which causes "whitening" of the images. In this study, we propose a semi-empirical technique that detects clouds by comparing an observation with a virtual clear-sky image at the appropriate sun elevation constructed from a database of real clear-sky images. Using the clear-sky image, we can take into account the inhomogeneity of the sky radiance distribution, and reduce errors that arise from the degradation of Charge Coupled Device (CCD) cameras. Our detection method allows the classification of sky types using red–green–blue (RGB) spectral features. We applied our detection method to images obtained with an all-sky camera system at Ny-Ålesund in May for the years 2005–2007. We then compared the detected clouds with cloud measurements using a Micro-Pulse Lidar (MPL) system. In this paper, we describe the details of this procedure and demonstrate the effectiveness of the proposed method.

2. Instrumentation

We used the PSV-100 All-Sky Camera (ASC) system manufactured by Prede Co., Ltd., Japan, to obtain whole-sky color images. The PSV-100 model consists of an all-sky camera unit with a blade (a device to shield from direct sunlight). In the camera unit, a fisheye lens is mounted on a camera that has a field of view of up to $160°$. The image sensor is a 1/$3''$ type color CCD, adjusted for daylight. The whole-sky images were taken at 10-min intervals, and saved in an 8-bit JPEG format with a maximum of 380,000 pixels. The blade to block off direct sunlight rotates automatically to track the solar orientation, which was calculated from the observation time, longitude, and latitude. It was necessary to analyze an average of 3×3 pixels to take into account the variations in pixel intensity when detecting optically thin clouds. For classification of the sky types in this paper, we used the 2086 hourly images (93.5% in total hours) observed at Ny-Ålesund during May of 2005–2007.

As described in the following sections, we used MPL data to determine the cloud detection thresholds. The MPL is an autonomous laser radar system developed in 1992 at the National Aeronautics and Space Administration (NASA) Goddard Space Flight Center (GSFC) (Spinhirne, 1993). The MPL system we used had optics and detector assemblies upgraded by NASA based on products manufactured by Science & Engineering Services, Inc. (SESI), USA, and had a measurement wavelength of 523 nm. The system has low transmitted pulse energies of 5−10 μJ with a 20 cm Schmidt−Cassegrain transmitter/receiver (transceiver) aperture and 2500 Hz laser pulse repetition frequency (Campbell et al., 2002). Data averaged over each minute were acquired with a 30 m range resolution.

The National Institute of Polar Research (NIPR) promotes atmospheric research in both Arctic and Antarctic regions. In the Arctic, the ASC is installed at the Rabben Observatory, a Japanese research base in Ny-Ålesund, Svalbard (78°56′N, 11°52′E, 40 m a.s.l.), while the MPL system is operated at the French and German Arctic research base (the German Alfred Wegener Institute for Polar and Marine Research, and the French Polar Institute Paul Emile Victor, AWIPEV) at Ny-Ålesund (Shiobara et al., 2006), approximately 1.4 km from the ASC location. In the Antarctic, the ASC and MPL systems are installed at Syowa Station (69°00′S, 39°35′E, 30 m a.s.l.).

3. Methodology

The detection method makes use of the spectral contrast between the RGB components of the ASC color image. That is, when the sky is clear, it appears deep blue because of the high spectral contrast between the blue and red components. Under cloudy conditions, clouds appear white or gray because the spectral contrast is rather flat owing to the optically (more opaque) thicker clouds. In this method, we assume that air molecules and aerosols other than clouds are uniformly distributed, and that their scattering is uniquely determined by the position of the sun, so that the clear sky radiance is independent of azimuth. We restricted the analysis area of the image zenith angle (IZA) to within 70°, because the high intensity of the ASC image near the horizon caused by the low sun elevation and the high surface albedo in polar regions results in inaccuracies when the proposed method is used (see Section 3.2). We used images taken when the SZA was lower than 85° because of the low sensitivity of the CCD camera at high SZA. Therefore, the method proposed in this paper is applicable for less than half the year in polar regions.

The analysis method for cloud detection from ASC images is summarized in the flowchart in Fig. 1. First, two images are prepared: the original whole-sky image and the virtual cloud-free image with the same SZA. The flowchart has three endpoints: (1) ASC-no-cloud (*clear* sky), (2) ASC-cloud-A (optically thick cloud or very bright cloud), and (3) ASC-cloud-B (optically thin cloud). Tests for pixels in the class ASC-no-cloud are applied at the beginning of the procedure. For the pixels that are not classified as clear sky, several tests
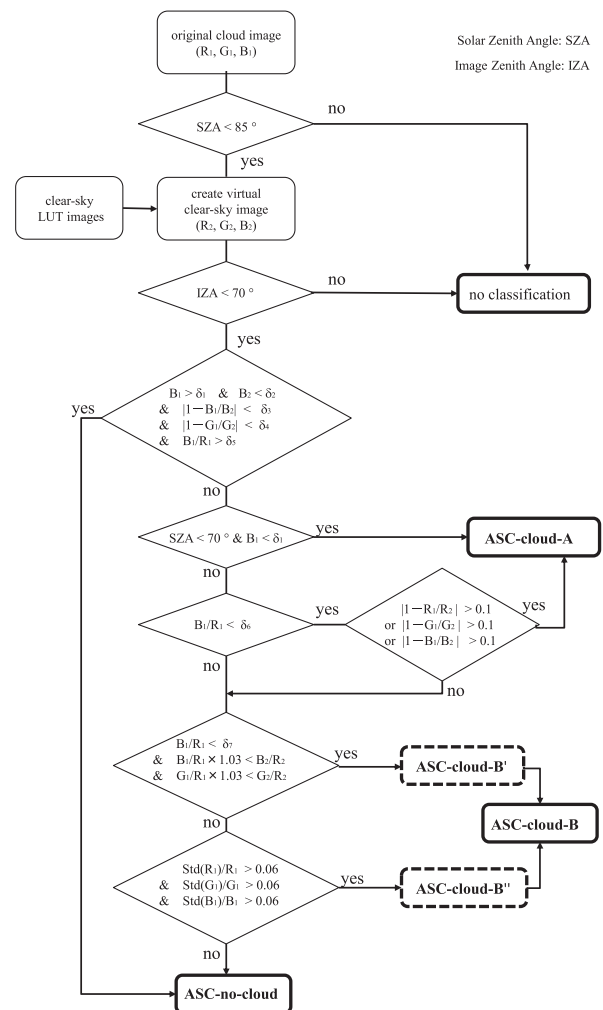

Fig. 1. Flowchart for the cloud detection method. The procedure starts by comparing the original whole-sky image and the virtual cloud-free image at the same solar zenith angle (SZA). The flowchart steps lead to three targets: (1) ASC-no-cloud (clear sky), (2) ASC-cloud-A (optically thick cloud or very bright cloud), and (3) ASC-cloud-B (optically thin cloud). Acronyms such as IZA are explained in the text.

Table 1
Cloud detection threshold values (δ_1–δ_7) for whole-sky images at the Arctic Ny-Ålesund Station (78°56′N, 11°52′E) and the Antarctic Syowa Station (69°00′S, 39°35′E).

Criteria	Ny-Ålesund	Syowa
δ_1	50	50
δ_2	190	190
δ_3	0.08	0.08
δ_4	0.07	0.08
δ_5	2.20	2.00
δ_6	1.35	1.35
δ_7	1.80	1.80

are used to identify ASC-cloud-A. For the pixels that are not classified as clear sky or ASC-cloud-A, tests are used to identify ASC-cloud-B, which is further divided into ASC-cloud-B′ and ASC-cloud-B″. Any remaining pixels are classified as ASC-no-cloud. The criteria from δ_1 to δ_7 (Table 1) and other specific values are determined by comparing lidar measurements with the results of the ASC data analyses in Figs. 5–7.

Fig. 2 shows a schematic flow of the cloud detection method applied to an image obtained on 31 May 2005 at Ny-Ålesund, with a SZA of 60.85°. First, we constructed the virtual clear-sky image with a SZA of
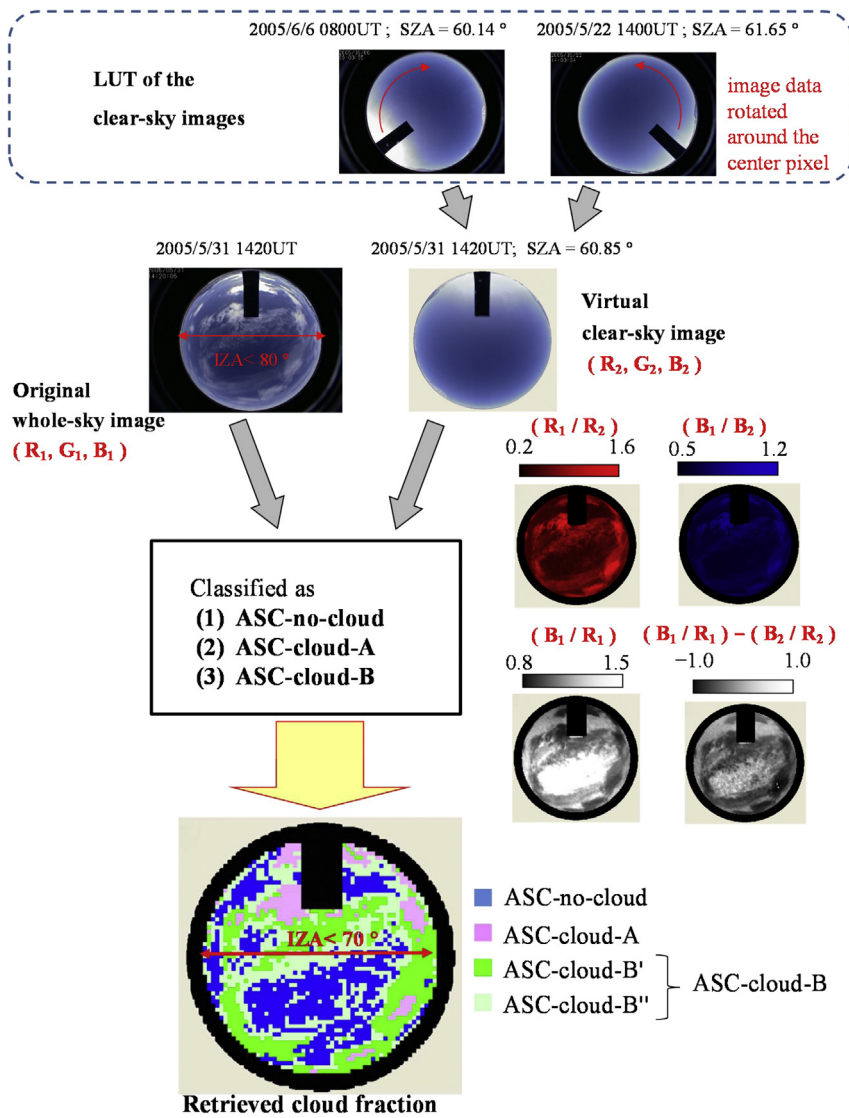

Fig. 2. Schematic flow of the cloud detection method applied to an example image obtained in May 2005 at Ny-Ålesund. The final detected cloud image is shown at the bottom, in which the image pixels are classified into three categories, (1) ASC-no-cloud (blue), (2) ASC-cloud-A (pink), and (3) ASC-cloud-B (green and light green).
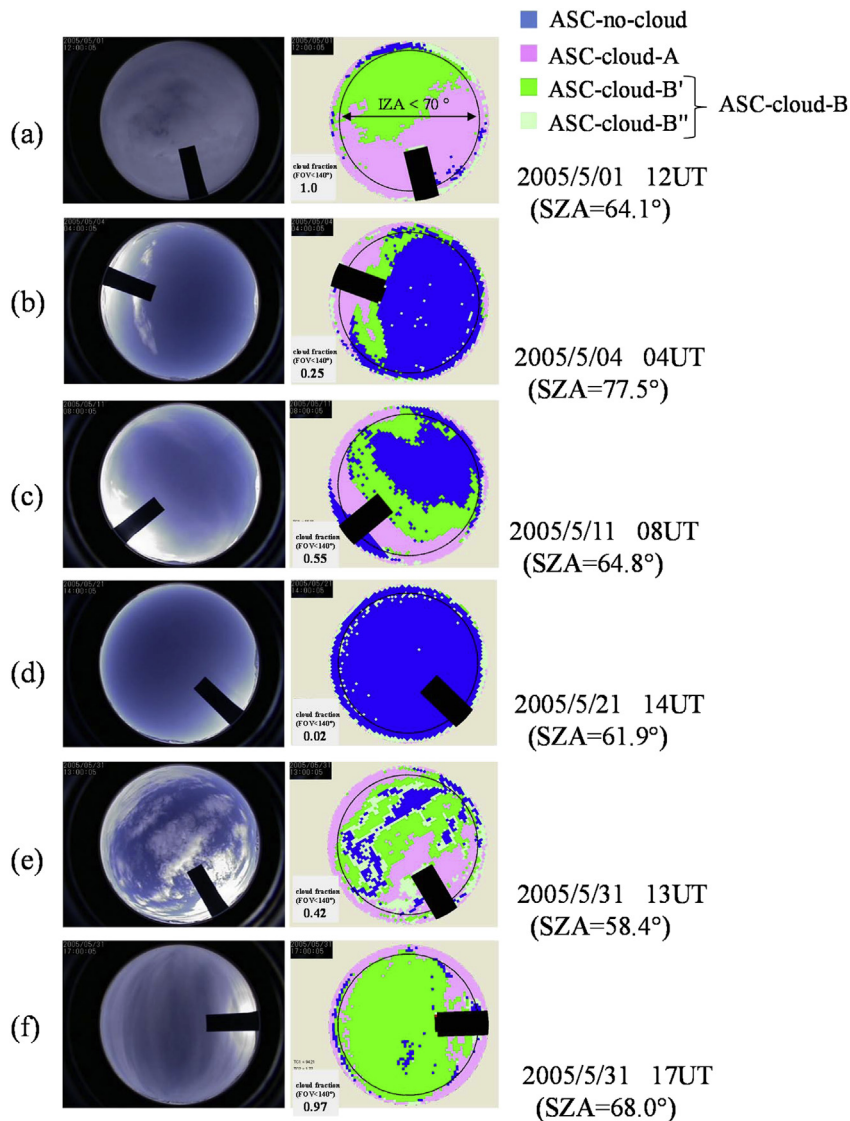
Fig. 3. Examples of whole-sky ASC images obtained in May 2005 at Ny-Ålesund (left panels), and the classified sky-type images derived from the proposed method (right panels). The sky types are classified as ASC-no-cloud (blue), ASC-cloud-A (pink), and ASC-cloud-B, which is further divided into ASC-cloud-B′ (green) and ASC-cloud-B″ (light green). The black circle in the sky-type images corresponds to IZA = 70°. The proposed method is effective only for IZA <70°, but results applied to the whole-sky images (IZA <80°) are shown to illustrate the limitation of the sky type classification.

60.85° using pixel-by-pixel interpolation between two observed clear-sky images with SZA of 60.14° (0800 UTC, 6 June 2005) and 61.65° (1400 UTC, 22 May 2005). The RGB values in the JPEG images were extracted from the original (R_1, G_1, B_1) and virtual images (R_2, G_2, B_2). The original and virtual images were then compared to detect different cloud categories and the retrieved image shows: (1) ASC-no-cloud (*clear* sky) in blue, (2) ASC-cloud-A (optically *thick* cloud or very *bright* cloud) in pink, and (3) ASC-

cloud-B (optically *thin* cloud) which is divided into ASC-cloud-B′, green, and ASC-cloud-B″, light green. Four supplemental images labeled (R_1/R_2), (B_1/B_2), (B_1/R_1), and (B_1/R_1) − (B_2/R_2) are included in this figure to aid in understanding the flowchart in Fig. 1.

Typical examples of the whole-sky ASC images obtained in May 2005 at Ny-Ålesund (left panels), and the classified sky type images derived from the proposed method (right panels) are presented in Fig. 3. The black circle in the sky-type images corresponds to
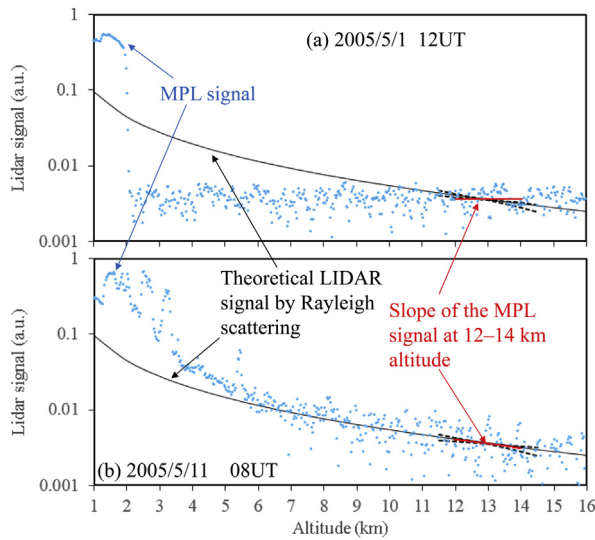
Fig. 4. Examples of the vertical profiles of the MPL return signals (blue circles) classified as MPL-cloud-I (a) and MPL cloud-II (b), corresponding to the sky images shown in Fig. 3(a) and (c), respectively. We obtained the slope of the height-dependent signals between altitudes of 12 and 14 km (red solid line) by using the least-squares method. The theoretical slope of Rayleigh scattering (black solid line) is fitted by the MPL signal at 13 km altitude. Black dotted lines indicate the 50% difference from the theoretical Rayleigh slope at 12–14 km altitude centered at 13 km.
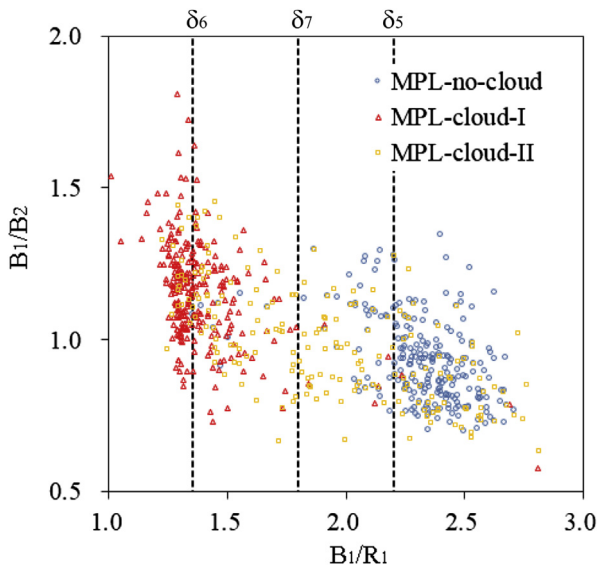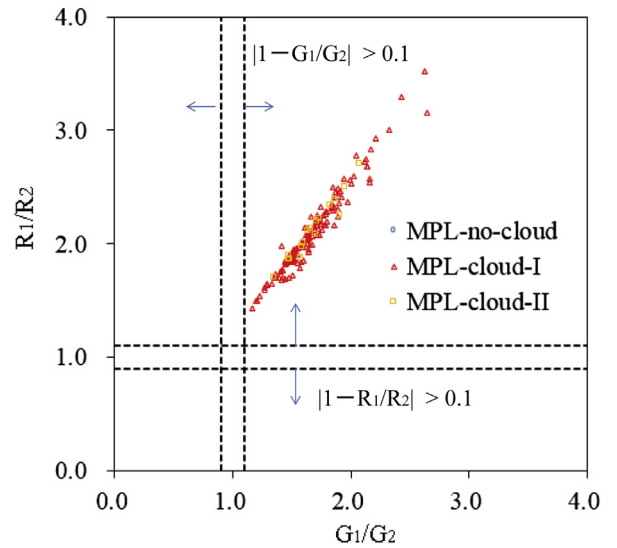

Fig. 6. The relationship of the ratios R_1/R_2 and G_1/G_2 of the pixels in the zenith direction for the target and virtual images, after pixels are extracted using the B_1/R_1 threshold value of δ_6. The points are categorized as MPL-no-cloud (blue circles), MPL-cloud-I (yellow squares), and MPL-cloud-II (red triangles). The MPL-no-cloud case disappears when the B_1/R_1 discrimination threshold is applied. The horizontal and vertical dashed lines correspond to the criteria $1 - R_1/R_2 = \pm 0.1$ and $1 - G_1/G_2 = \pm 0.1$. The pixels classified as ASC-cloud-A are detected when either $|1 - R_1/R_2| > 0.1$ or $|1 - G_1/G_2| > 0.1$.

Fig. 5. The relationship between the ratios B_1/B_2 and B_1/R_1 of the pixels in the zenith direction (IZA = 0) from hourly data observed at Ny-Ålesund in May 2005. The colors correspond to the sky categories of MPL-no-cloud (blue circles), MPL-cloud-I (yellow squares), and MPL-cloud-II (red triangles). The three vertical dashed lines correspond to the threshold values from δ_5 to δ_7 in the detection flowchart of Fig. 1.

an IZA of 70°. The proposed method is effective only within an IZA of 70°, but the results applied to the whole-sky images (IZA <80°) are shown to illustrate the limitation of the sky type classification. In the following sections, we will describe in more detail the procedures of the detection method shown in Figs. 1 and 2.

3.1. Virtual clear-sky images

We compiled a look-up table (LUT) of whole-sky images during entirely cloud-free weather, selected at given solar zenith angles with increments of several degrees. ASC images within an IZA of 80° are determined to be entirely cloud-free by a visual check as well as by MPL cloud detection analysis for a period with no clouds that lasts for 1 h. We did not consider the azimuthal dependence of scattering, so for the sake of simplicity, the LUT was constructed using image data rotated around the center pixel (so that the IZA is 0°). Clear-sky images with a wide range of SZAs are required for the database. In addition, the clear-sky images must be updated according to location and analysis period to capture seasonal variations of sky radiance caused by ground conditions, aerosol optical
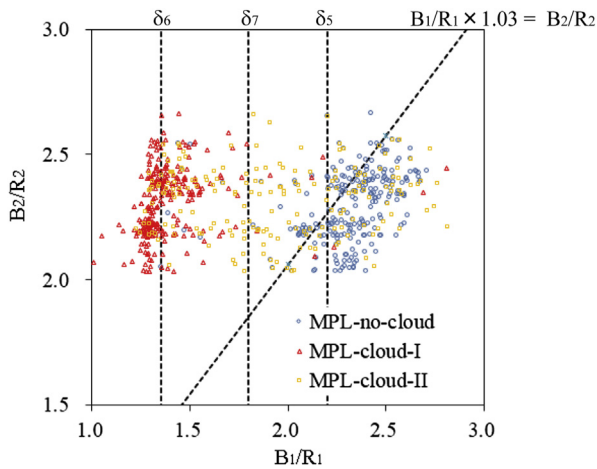
Fig. 7. The relationship of the ratios B_2/R_2 and B_1/R_1 of the pixels in the zenith direction (IZA $= 0°$), from the target and virtual images. The points are categorized as MPL-no-cloud (blue circles), MPL-cloud-I (yellow squares), and MPL-cloud-II (red triangles). The diagonal dashed line corresponds to the relationship $B_2/R_2 = 1.03 \times B_1/R_1$.

properties, and sensitivity fluctuations of the CCD. Because the reference cloud-free images are acquired at different times under differing aerosol optical properties and surface albedo, misclassification can occur for images obtained under other very different conditions (e.g., a strong haze event). To analyze the images obtained in May, we used the 15 clear-sky images taken around May with SZAs nearly equally spaced between $88.8°$ and $55.5°$.

Next, we created a virtual clear-sky image for the solar zenith angle corresponding to the observation time, latitude, and longitude of the original image. The virtual clear-sky image is created by selecting two images from the LUT at zenith angles that are closest to the original image, and linearly interpolating the pixel RGB values.

3.2. Detection of clouds

As shown in Fig. 2, a threshold is determined from the RGB values of the original (R_1, G_1, B_1) and virtual (R_2, G_2, B_2) clear-sky images to classify pixels into (1) ASC-no-cloud, (2) ASC-cloud-A, or (3) ASC-cloud-B. We used cloud types estimated from the MPL measurements to determine the threshold values in Table 1.

The presence or absence of cloud is determined by using cloud base height analysis of the MPL signal. The MPL signal corrections and cloud base height detections were determined using methods described in Welton and Campbell (2002) and Campbell et al.

(2002, 2008) after integrating the signal for 10 min. When a cloud base height below 10 km can be detected in the MPL profile, we define the profile as MPL-cloud; otherwise the profiles are classified as MPL-no-cloud. For comparison with the sky types categorized by ASC, MPL-cloud is further divided into two categories on the basis of optical attenuation and background noise.

If cloud is present, it is classified as optically thin or thick. Shiobara et al. (2003) determined the optical characteristics of clouds using the slope of signal attenuation after penetration into the cloud. However, it is difficult to use this technique for multi-layer clouds. In this study, we took advantage of the signal near the tropopause, which is less affected by Mie scattering of aerosols and clouds. This is because the luminance values of the whole-sky image reflect the atmospheric conditions of the integrated air column. MPL can measure thick aerosol layers and multilayered clouds through the troposphere if the slope of the MPL signal near the tropopause consists of signal attenuation by Rayleigh scattering.

In this analysis, we compared the actual slope of the MPL signal at $12-14$ km altitude and the theoretical slope obtained with Rayleigh scattering calculated from the vertical profile model of the atmosphere appropriate to the subarctic summer (McClatchey et al., 1972). We obtained the slope of the height-dependent signals between altitudes of 12 and 14 km by using the least-squares method.

Clouds detected by the cloud base height analysis are classified as MPL-cloud-I when the MPL signal slope is not valid at $12-14$ km altitude because of high noise, regardless of the type of optical attenuation. The MPL-cloud-I class includes optically thick single- and multi-layer clouds, as well as the partially cloud-filled case with very bright clouds due to the strong scattered solar beam that causes the high background noise. This effect is obvious for clouds close to the sun. [Or would you prefer 'close to'?] Conversely, clouds are classified as MPL-cloud-II when the MPL signal slope near the tropopause agrees with the expected signal attenuation by Rayleigh scattering. We defined the MPL signal profile as valid when the difference between the observed and modeled slopes at $12-14$ km altitude was less than 50% of the modeled value.

Fig. 4 shows the vertical profiles of the MPL return signal classified as MPL-cloud-I (a) and MPL cloud-II (b), corresponding to the sky images shown in Fig. 3(a) and (c), respectively. The observed slope at 13 km altitude is fitted to the theoretical Rayleigh scattering slope. For the case categorized as MPL-cloud-I shown

in Fig. 4(a), the slope of the MPL return signal above 2 km altitude was close to unity due to strong attenuation by the optically thick cloud layer below 2 km. Conversely, the return signal classified as MPL-cloud-II shown in Fig. 4(b) exhibited a slow decrease with height after penetrating multi-layer clouds between 1 and 6 km, although the signal fluctuates strongly due to attenuation of the laser light in cloud layers. Then, by comparing the difference between the observed and theoretical Rayleigh slopes at 12—14 km altitude, we judged whether the MPL signal profile is valid.

There are cases where analysis of the MPL signal slope indicates MPL-cloud-I clouds, even though the cloud base height detection method does not detect cloud. These cases are caused by very low cloud or fog, which cannot be detected by MPL due to overlap between the laser beam and the receiver field-of-view; some system problems such as low laser power and the presence of obstacles (e.g., snow on the window) in front of the MPL field-of-view give the same effect. These cases where there is a mismatch between the cloud-base detection and the slope of the attenuation of the signals at 12—14 km altitude make up less than 0.5% of the data obtained in May of 2005—2007 at Ny-Ålesund. If the optically thick clouds are dominant for very low clouds, the cloud detection accuracy is only slightly affected by the MPL overlap problem. In this paper, we omitted this type of mismatch case from the analysis. We defined MPL-cloud-I as the indicator of optically thick clouds and very bright clouds, and MPL-cloud-II as thin cloud that can be penetrated by the MPL laser beam.

The background noise in the MPL measurements is high during the daytime when whole-sky images are available. Therefore, it is difficult to quantify the cloud optical properties because they depend strongly on the optical characteristics of the atmospheric constituents and the intensity of background light. However, previous studies have proposed criteria for measuring clouds using MPL. For instance, based on the comparison between MPL and Raman Lidar measurements over the ARM Southern Great Plains site, Dupont et al. (2011) suggested that only 20% of optically thick cirrus clouds (optical thickness >0.3) are detected up to cloud top by MPL due to the low pulse energy and the effect of solar irradiance contamination.

3.2.1. Detection of ASC-no-cloud

First, we extracted only the obvious ASC-no-cloud pixels from the image. In this procedure, we did not target pixels with an insufficient color ratio caused by lower brightness at lower sun elevation, or with higher or saturated brightness in red, green, or blue around the sun. To identify clear sky (ASC-no-cloud) in the first stage of the flowchart in Fig. 1, thresholds (δ_1, δ_2) are provided for B_1 and B_2. While using the criterion $B_1 > \delta_1$ eliminates the dark pixels from the original images, the higher or saturated brightness pixels around the sun are removed using the criterion $B_2 < \delta_2$. These thresholds depend on the measurement location and CCD sensitivity. After confirming that there is sufficient sensitivity, we checked whether the luminance ratio of B_1 to B_2, or of G_1 to G_2, is close to unity; that is, whether the original pixels are close to the virtual clear-sky ones. Here, we defined the values of B_1/B_2 and G_1/G_2 for the ASC-no-cloud pixels as satisfying $|1 - B_1/B_2| < \delta_3$ and $|1 - G_1/G_2| < \delta_4$, respectively. In general, the fluctuations of $|1 - B_1/B_2|$ and $|1 - G_1/G_2|$ for visually classified no-cloud pixels tend to be below 10%. In addition, if the color ratio of B_1 to R_1 is higher than a given threshold δ_5, clear sky (ASC-no-cloud) is detected. Fig. 5 shows the relationship between the ratios B_1/B_2 and B_1/R_1 of the pixels in the zenith direction from the hourly data observed at Ny-Ålesund in May 2005. The colors of the plots correspond to the three different classes based on the MPL measurements. In Fig. 5, a clear distinction can be seen for the values of B_1/R_1 for MPL-no-cloud. In Fig. 5, the threshold δ_5 used in the flowchart of Fig. 1 was taken from Table 1 (2.20 for ASC-no-cloud). Three thresholds (δ_3, δ_4, δ_5) were used to determine whether or not several no-cloud images for the various solar zenith angles could be classified as ASC-no-cloud. Any pixels remaining unclassified after the ASC-cloud-A and ASC-cloud-B detection procedures are classified as ASC-no-cloud. The results that apply for the clear-sky image are shown in Fig. 3(d). The pixels that almost qualify in Fig. 3(d) are categorized as ASC-no-cloud, except for a few pixels near the horizon.

3.2.2. Detection of ASC-cloud-A

ASC-cloud-A corresponds to optically thick grayish clouds, or clouds illuminated by scattered light. First, we determined the presence of cloud with low luminance despite a SZA below 70°. We used $B_1 \leq \delta_1$ to identify the dark pixels in the detection procedure for ASC-no-cloud as described in Section 3.2.1. This corresponds to, for example, an optically very thick cloud covering the whole sky with heavy rain or snow.

Next, we examined the color ratio B_1/R_1 to detect optically thick cloud or illuminated cloud, such as the pixels around the sun disk with low spectral contrast. In general, clouds and aerosols enhance red versus blue

intensity, increasing the red—blue ratio compared to the clean cloud-free atmosphere (Shields et al., 1993). The B_1/R_1 threshold of δ_6 in the flowchart of Fig. 1 was used to classify pixels as MPL-cloud-I, as shown in Fig. 5. A value of 1.35 was chosen for δ_6 to define ASC-cloud-A ($B_1/R_1 < 1.35$). However, lower values of the color ratio B_1/R_1 sometimes occur in clear-sky cases, especially around the sun disk and close to the horizon, as well as in cases where clouds appear illuminated due to image saturation by high intensity radiation. We then employed the ratios R_1/R_2, G_1/G_2, and B_1/B_2 to distinguish between cloud and clear-sky pixels. In the absence of cloud pixels, the luminance ratios between the original picture and the virtual clear-sky image for each color (i.e., R_1/R_2, G_1/G_2, and B_1/B_2) will be closer to unity, independent of B_1/R_1. Fig. 6 illustrates the ratios R_1/R_2 and G_1/G_2 of pixels in the zenith direction for the MPL-classified sky types, after the pixels have been extracted using the B_1/R_1 threshold value of δ_6. The MPL-no-cloud case is completely eliminate by the B_1/R_1 discrimination threshold. Cloud classification using the red—blue ratio in the zenith direction should give more appropriate results than near the horizon, where the brighter and whiter pixels are found. We determined the permissible range for pixels to be categorized as ASC-cloud-A by referring to the results in the zenith direction, as illustrated in Fig. 6. Here, pixels are classified as ASC-cloud-A when any of $|1 - R_1/R_2| > 0.1$, $|1 - G_1/G_2| > 0.1$, or $|1 - B_1/B_2| > 0.1$ is satisfied. We used magnitude rather than actual value, because the relationship between (R_1, G_1, B_1) and (R_2, G_2, B_2) is sometimes reversed when a cloud appears reddish from being lit by a low altitude sun.

Some sample images are shown in Fig. 3. For the case of an optically very thick cloud covering the whole sky, Fig. 3(a), more than half the pixels are classified as ASC-cloud-A with IZA $<70°$. The illuminated clouds are classified as ASC-cloud-A as shown by Fig. 3(b), (c), (e), and (f). On the other hand, there are misclassifications of ASC-no-cloud in the range $70° \leq$ IZA $< 80°$ when the proposed method is used for cases (a), (c), and (f) in Fig. 3, because the high intensity in the ASC image near the horizon caused by the low sun elevation and the high surface albedo in polar regions results in inaccuracies. Therefore, we restricted the area of analysis to IZA $\leq 70°$.

3.2.3. Detection of ASC-cloud-B

At the next stage of the flowchart in Fig. 1, we detect optically thin clouds (ASC-cloud-B), using pixels that were not previously identified as clear sky,

optically thick clouds, or illuminated clouds. Note that ASC-cloud-B is divided into two categories, ASC-cloud-B′ and ASC-cloud-B″.

First, we define ASC-cloud-B′. Fig. 7 shows the relationship between the ratios B_2/R_2 and B_1/R_1 for pixels in the zenith direction. We define the threshold δ_7 of B_1/R_1 so that clear sky is not mistaken for thin clouds, as there is a large overlap between the distribution of the MPL-no-cloud and MPL-cloud-I cases shown in Fig. 5. The δ_7 value is close to the midpoint of δ_5 and δ_6. In previous research, using a unique threshold for the blue and red signals, Long et al. (2006) reported that the best threshold value to separate cloudy and cloudless areas was R/B = 0.6 (B/R = 1.67). Kreuter et al. (2009) found that B/R = 1.3 was a suitable threshold for marking cloudy pixels. These thresholds are similar to our values of δ_7 for ASC-cloud-B, and δ_6 for ASC-cloud-A. On the other hand, Heinle et al. (2010) employed the difference R − B = 30, rather than the ratio R/B. This corresponds approximately to our criteria of δ_5 for ASC-no-cloud and δ_6 for a part of ASC-cloud-A, since this criterion is effective when there is a large difference between red and blue signals, including brighter pixels.

The relationship of the color ratios between the virtual clear sky and observed whole-sky images (such as B_2/R_2, B_1/R_1, G_2/R_2, and G_1/R_1) also contributes to the precise detection of optically thin clouds. When clouds are present, the spectral contrast of the cloud pixels becomes low compared with the clear sky cases, reflecting the different optical properties of the molecules and cloud particles. Here, we classified ASC-cloud-B′ using a criterion based combination of $(B_2/R_2, B_1/R_1)$ and $(G_2/R_2, G_1/R_1)$ as well as the threshold B_1/R_1. This classification is valid for optically thin clouds that can be clearly identified by eye from images (e.g., pixels not located around the sun direction of Fig. 3(b), (c), (e), and (f)).

Next, we classified ASC-cloud-B″, which is difficult to determine on the basis of spectral contrast and comparison of the original and virtual clear-sky images. It is useful to examine the standard deviation of each color to detect any uniformly distributed cirrus clouds, which are not always identified by the previous procedures. We used an average and standard deviation over 3×3 pixels to take into account the variance between the pixels. We defined ASC-cloud-B″ when the coefficient of variance for each color is greater than 0.06. This criterion is useful for the inhomogeneous thin clouds shown in Fig. 3(e). However, the discrimination of sky types close to the sun in the presence of very thin cirrus clouds or of an aerosol-rich air mass is

Table 2
Classification matrix of sky types based on the MPL and ASC observations derived from 2086 h of data obtained for May 2005—2007 at Arctic Ny-Ålesund Station. Here, the ASC data refer to 3 × 3 pixel areas in the zenith direction (IZA = 0).

Sky types	MPL-no-cloud	MPL-cloud-I	MPL-cloud-II
ASC-no-cloud	529 h (25.4%)	28 h (1.3%)	214 h (10.3%)
ASC-cloud-A	5 h (0.2%)	559 h (26.8%)	67 h (3.2%)
ASC-cloud-B	40 h (1.9%)	398 h (19.1%)	246 h (11.8%)

still problematic (e.g., pixels close to the sun in Fig. 3(b) and (c)).

Finally, the pixels that were not classified as clear sky (ASC-no-cloud), optically thick cloud, very bright cloud (ASC-cloud-A), or optically thin cloud (ASC-cloud-B) were classified as ASC-no-cloud. That is, ASC-no-cloud includes unclassified pixels as well as clear-sky pixels.

4. Validation with MPL measurements

We applied our detection method to the 2086 hourly ASC images that we obtained in May for the years 2005—2007 at Ny-Ålesund, and compared the results with the MPL cloud measurements. Table 2 summarizes the classification matrix of sky types based on the MPL and ASC observations. Here, the ASC data were averaged over 3 × 3 pixels in the zenith direction (IZA = 0). When MPL did not detect any clouds (i.e., MPL-no-cloud), the false cloud detection rate from ASC was 2.1% (0.2% for ASC-cloud-A and 1.9% for ASC-cloud-B). On the other hand, the ASC classification indicated no-cloud for 11.6% of the cloud cases detected by MPL (1.3% for MPL-cloud-I and 10.3%

for MPL-cloud-II). These results suggest that the proposed ASC classification is valid for the optically thick clouds or the illuminated clouds categorized as MPL-cloud-I, but sometimes underestimates the optically thin clouds categorized as MPL-cloud-II.

Fig. 8 shows a comparison of the results using ASC and MPL, when MPL has classified the cloud as MPL-cloud-I or MPL-cloud-II. In addition, Fig. 8 includes the frequency distribution of the cloud base height at 1-km height intervals measured with MPL, with details of the corresponding ASC cloud types obtained using our method. When MPL detects clouds of type MPL-cloud-I, they are likely to be low-level clouds that are classified as either ASC-cloud-A or ASC-cloud-B (with a ratio of 6:4 in Fig. 8(a)). Conversely, MPL-cloud-II cases are distributed up to 10 km because of the dominance of optically thin clouds such as cirrus clouds, and are mostly classified as ASC-no-cloud or ASC-cloud-B by the ASC cloud detection method as shown in Fig. 8(b). If we improve the sensitivity of the ASC method so as to detect more thin clouds, then the criteria for ASC-cloud-B will change. This improvement, however, would lead to an underestimation of clear-sky pixels, as there is a large overlap between the distributions of MPL-no-cloud and MPL-cloud-I plots shown in Figs. 5 and 7. Therefore, the result as shown in Fig. 8(b) seems reasonable because ASC is not sensitive to very thin clouds. In addition, we have confirmed that heavy haze layers can be misclassified as cirrus clouds in a whitish sky for the mismatched cases in the MPL-no-cloud–ASC-cloud-B combination. Furthermore, the 1.4 km distance between the locations of the ASC and MPL systems may cause
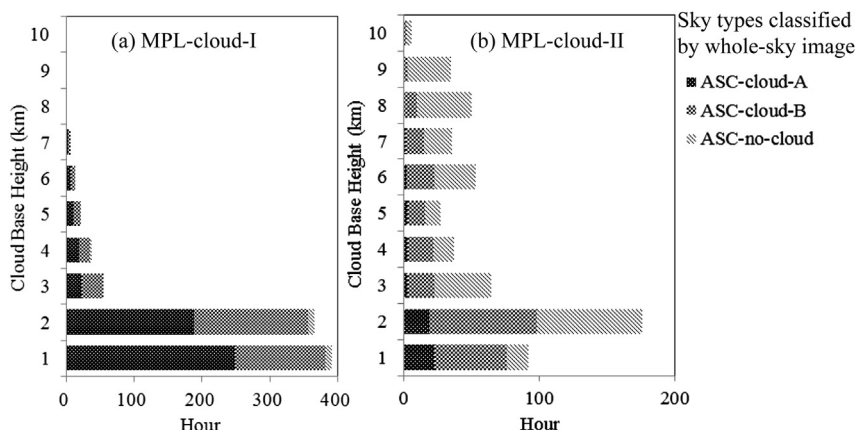

Fig. 8. Validation of the ASC detection method using MPL results. These figures show the relationship between cloud base height and ASC observation hours (i.e., the number of ASC images) when the MPL system identified MPL-cloud-I (a), and MPL-cloud-II (b) clouds. Sky types ASC-cloud-A, ASC-cloud-B, and ASC-no-cloud are shown by dark, medium, and light shading, respectively.
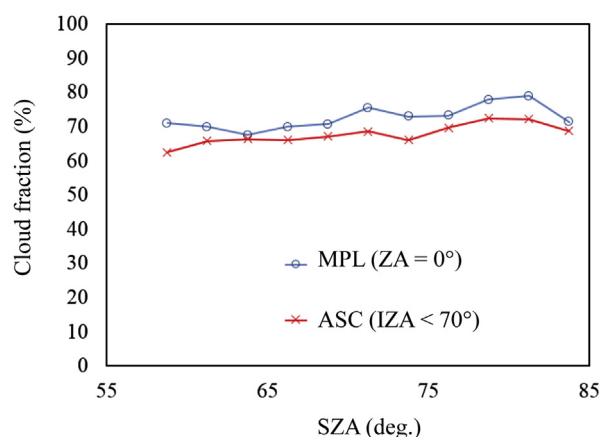
Fig. 9. The SZA dependence of the averaged cloud fractions derived from MPL (blue line) and ASC images with IZA <70° (red line) obtained in May of 2005–2007 at Ny-Ålesund.

some errors, because of the time lag for intermittent passing clouds.

When applying the proposed sky-type classification method to different seasons, it is important to note whether the accuracy of the retrieved results depends on the SZA. Fig. 9 shows the SZA dependence of the averaged cloud fractions derived from MPL in the zenith direction, and the ASC images with IZA <70° obtained in May of the years 2005–2007 at Ny-Ålesund. Though the cloud fractions retrieved from ASC images were somewhat lower than the MPL cloud fractions described in Table 2, the variability of the cloud fractions for MPL and ASC was roughly constant regardless of SZA. This confirms that the method developed in this study is valid for cloud detection using wohle−sky color images for the SZA range characteristic of polar regions.

Finally, Table 1 summarizes the values of $\delta_1-\delta_7$ used in the analysis of ASC images for Ny-Ålesund, Svalbard, and Syowa Station, Antarctica. Because the detection scheme is the same, the parameters are almost identical except for δ_4 and δ_5, the threshold used for the ASC-no-cloud pixels.

5. Summary

We have proposed a technique for the detection of clouds from whole-sky color images observed with an all-sky camera system. This method uses the differences between real images and virtual clear-sky images for the observation time. In this paper, the sky types from the ASC image are categorized as (1) ASC-no-cloud (clear sky), (2) ASC-cloud-A (optically thick cloud or very bright cloud), and (3) ASC-cloud-B (optically thin

cloud). We applied the method using 3×3 pixel areas in the zenith direction from ASC images obtained at Ny-Ålesund, Svalbard in May of the years 2005–2007, and compared our results with MPL measurements. Our results show that when no clouds were estimated by MPL, the false cloud detection rate from ASC was 2.1%. Conversely, the ASC method underestimated the cloud by 11.6% when clouds were detected by MPL. In most cases, this difference occurred when MPL detected optically very thin clouds. This suggests that ASC images are less sensitive to very thin clouds than MPL, which is an active remote sensing system. Furthermore, we examined the SZA dependence of the accuracy of the cloud fractions retrieved from ASC images and confirmed that the variability of the cloud fractions between MPL and ASC was roughly constant regardless of the SZA. Thus, it is confirmed that the method developed in this study is valid for cloud detection from whole-sky color images.

Although cloud cover is one of the most influential components in the earth's radiation budget, our knowledge of clouds is still insufficient. It is generally recognized that the lack of scientific understanding of clouds may cause large uncertainties in numerical predictions of future climate. Therefore, we need to investigate cloud characteristics precisely and accurately, especially in polar regions, where global climate change may be magnified (IPCC, 2013). We believe that cloud analysis using all-sky camera data can contribute to the understanding of cloud effects on the polar climate. Also, cloud detection from ground-based instruments, including all-sky camera systems, can contribute to ground validation of satellite retrievals of cloud characteristics in polar regions.

References

Alonso, J., Batlles, F.J., Villarroel, C., Ayala, R., Burgaleta, J.I., 2014. Determination of the sun area in sky camera images using radiometric data. Energy Convers. Manag. 78, 24−31.

Campbell, J.R., Hlavka, D.L., Welton, E.J., Flynn, C.J., Turner, D.D., Spinhirne, J.D., Scott, V.S., Hwang, I.H., 2002. Full-time, eye-

safe cloud and aerosol lidar observation at atmospheric radiation measurement program sites: instruments and data processing. J. Atmos. Oceanic Technol. 19, 431—442.

Campbell, J.R., Sassen, K., Welton, E.J., 2008. Elevated cloud and aerosol layer retrievals from micropulse lidar signal profiles. J. Atmos. Oceanic Technol. 25, 685—700.

Dupont, J.C., Haeffelin, M., Morille, Y., Comstock, J.M., Flynn, C.J., Long, C.N., Sivaraman, C., Newsom, R.K., 2011. Cloud properties derived from two lidars over the ARM SGP site. Geophys. Res. Lett. 38, L08814. http://dx.doi.org/10.1029/2010GL046274.

Feister, U., Möller, H., Sattler, T., Shields, J., Görsdorf, U., Güldner, J., 2010. Comparison of macroscopic cloud data from ground-based measurements using VIS/NIR and IR instruments at Lindenberg, Germany. Atmos. Res. 96, 395—407.

Hartmann, D.L., 1993. Radiative effects of clouds on earth's climate. In: Hobbs, P.V. (Ed.), Aerosol—Cloud—Climate Interactions, International Geophysics, vol. 54. Academic Press, New York, pp. 151—173 chapter 6.

Heinle, A., Macke, A., Srivastav, A., 2010. Automatic cloud classification of whole sky images. Atmos. Meas. Tech. 3, 557—567.

IPCC, 2013. Climate Change 2013: The Physical Science Basis. Contribution of Working Group I to the Fifth Assessment Report of the Intergovernmental Panel on Climate Change. Cambridge University Press, Cambridge, United Kingdom and New York, NY, USA. http://www.ipcc.ch/report/ar5/wg1/.

Kazantzidis, A., Tzoumanikas, P., Bais, A.F., Fotopoulos, S., Economou, G., 2012. Cloud detection and classification with the use of whole-sky ground-based images. Atmos. Res. 113, 80—88.

Kreuter, A., Zangerl, M., Schwarzmann, M., Blumthaler, M., 2009. All-sky imaging: a simple, versatile system for atmospheric research. Appl. Opt. 48, 1091—1097.

Liu, L., Sun, X.J., Gao, T.C., Zhao, S.J., 2013. Comparison of cloud properties from ground-based infrared cloud measurement and visual observations. J. Atmos. Oceanic Technol. 30, 1171—1179.

Long, C.N., Sabburg, J.M., Calbó, J., Pagès, D., 2006. Retrieving cloud characteristics from ground-based daytime color all-sky images. J. Atmos. Oceanic Technol. 23, 633—652.

McClatchey, R.A., Fenn, R.W., Selby, J.E.A., Volz, F.E., Garing, J.S., 1972. Optical Properties of the Atmosphere. Report AFCRL-72-0497, Third ed. Air Force Cambridge Research Laboratories, Bedford, MA.

Raschke, E., Ohmura, A., Rossow, W.B., Carlson, B.E., Zhang, Y.C., Stubenrauch, C., Kottek, M., Wild, M., 2005. Cloud effects on the radiation budget based on ISCCP data (1991 to 1995). Int. J. Climatol. 25, 1103—1125.

Shields, J.E., Johnson, R.W., Koehler, T.L., 1993. Automated whole sky imaging systems for cloud field assessment. In: Proceedings of Fourth Symposium on Global Change Studies. American Meteorological Society, Boston, MA, pp. 228—231.

Shields, J.E., Johnson, R.W., Karr, M.E., Wertz, J.L., 1998. Automated day/night whole sky imagers for field assessment of cloud cover distributions and radiance distributions. In: Proc. 10th Symp. on Meteorological Observations and Instrumentation, 11—16 January 1998. American Meteorological Society, Boston, MA, pp. 165—170.

Shields, J.E., Karr, M.E., Johnson, R.W., Burden, A.R., 2013. Day/night whole sky imagers for 24-h cloud and sky assessment: history and overview. Appl. Opt. 52, 1605—1616.

Shiobara, M., Yabuki, M., Kobayashi, H., 2003. A polar cloud analysis based on Micro-pulse Lidar measurements at Ny-Ålesund, Svalbard and Syowa, Antarctica. Phys. Chem. Earth 28, 1205—1212.

Shiobara, M., Yabuki, M., Neuber, R., Spinhirne, J.D., Welton, E.J., Campbell, J.R., Hart, W.D., Berkoff, T.A., 2006. Arctic experiment for ICESat/GLAS ground validation with a Micro-pulse Lidar at Ny-Ålesund, Svalbard. Polar Meteorol. Glaciol. 20, 28—39.

Spinhirne, J.D., 1993. Micro pulse lidar. IEEE Trans. Geo. Rem. Sens. 31, 48—55.

Thorsen, T.J., Fu, Q., Comstock, J.M., 2013. Cloud effects on radiative heating rate profiles over Darwin using ARM and A-train radar/lidar observations. J. Geophy. Res. 118, 5637—5654.

Welton, E.J., Campbell, James R., 2002. Micropulse lidar signals: uncertainty analysis. J. Atmos. Oceanic Technol. 19, 2089—2094.